

The giants that were born swiftly - Implications of the top-heavy stellar initial mass function on the birth conditions of globular clusters

Henriette Wirth^{1*}, Pavel Kroupa^{1,2}, Jaroslav Haas¹, Tereza Jerabkova³,
Zhiqiang Yan^{1,4} and Ladislav Šubr¹

¹Charles University, Faculty of Mathematics and Physics, Astronomical Institute, V Holešovičkách 2, Praha, CZ-18000, Czech Republic

²Helmholtz Institut für Strahlen und Kernphysik, Universität Bonn, Nussallee 14/16, 53115 Bonn, Germany

³European Southern Observatory, Karl-Schwarzschild-Strasse 2, 85748 Garching bei München

⁴School of Astronomy and Space Science, Nanjing University, Nanjing, 210023, China

Accepted XXX. Received YYY; in original form ZZZ

ABSTRACT

Recent results suggest that the **initial mass function (IMF)** of **globular clusters (GCs)** is metallicity and density dependent. Here it is studied how this variation affects the initial masses and the numbers of **core collapse supernovae (CCSNe)** required to reproduce the observed iron spreads in **GCs**. The **IMFs** of all of the investigated **GCs** were top-heavy implying larger initial masses compared to previous results computed assuming an invariant canonical **IMF**. This leads to more **CCSNe** being required to explain the observed iron abundance spreads. The results imply that the more massive **GCs** formed at smaller Galactocentric radii, possibly suggesting in-situ formation of the population II halo. The time until **star formation (SF)** ended within a proto-**GC** is computed to be 3.5 - 4 Myr, being slightly shorter than the 4 Myr obtained using the canonical **IMF**. Therefore, the impact of the **IMF** on the time for which **SF** lasts is small.

Key words: globular clusters: general – supernovae: general – stars: abundances – methods: analytical

1 INTRODUCTION

While most **globular clusters (GCs)** have been observed to be homogeneous with respect to iron (Carretta et al. 2009b; Mucciarelli et al. 2015; Montecinos et al. 2021), there is evidence for iron abundance spreads in some of them (Pancino et al. 2000; Ferraro et al. 2009; Lardo et al. 2016; Marino et al. 2018; Bailin 2019; Lardo et al. 2022). This spread in iron is believed to be caused by pollution through **core collapse supernovae (CCSNe)**, however, it is unclear at which stage of **GC** development these **CCSNe** exploded (D’Antona et al. 2016; Wirth et al. 2021; Lacchin et al. 2021). In Wirth et al. (2021, hereinafter Paper I) a novel method to estimate the number of **CCSNe** required to explain the iron abundance spread in a **GC** assuming that the iron spread is caused by **CCSN** was introduced. This approach was based on a model in which **GCs** without an iron spread arise if **star formation (SF)** stops before the first **CCSN** can pollute the gas in the **GC**. If **SF** continues past this point, the **CCSNe** will pollute the surrounding gas with iron, such that more iron rich stars form. Paper I shows how the number of **CCSNe** contributing to this iron rich population and the time after which **SF** ends can be computed using the iron spread catalogue from Bailin (2019).

An integral part of the calculations in Paper I was to compute the initial masses of the **GCs**. To this end we used a set of equations which Baumgardt & Makino (2003) derived from N-body simulations. The initial mass of a **GC** is, like other **GC** parameters, related to the assumed **initial mass function (IMF)** (Prantzos & Charbonnel 2006; Marks et al. 2012; Bekki et al. 2017; Jeřábková et al. 2017; Kalari et al. 2018; Schneider et al. 2018; Chon et al. 2021). In Paper I, the canonical **IMF** (Kroupa 2001; Kroupa et al. 2013) was assumed for all **GCs**. However, several theoretical (Sharda & Krumholz 2022) and observational (Marks et al. 2012; Zhang et al. 2018; Yan et al. 2021; Pouteau et al. 2022) studies have found that the **IMF** does change depending on the initial density and metallicity of a stellar population.

To determine the **IMF** of a **GC** is challenging since the mass function of a **GC** changes over time. This is mainly due to two effects: the fact that massive stars die first (see e.g. Portinari et al. 1998; Marigo 2001) and the loss of stars due to energy-equipartition driven evaporation and ejection (Fall & Zhang 2001; Heggie & Hut 2003; Webb & Leigh 2015). Additionally, mergers can play a role (Kravtsov et al. 2022).

Despite these obstacles, several attempts have been made to compute the **IMF** of a **GC**. Only recently, Webb & Bovy (2021) suggested to use the mass function observed at the ends of the tidal tails of a **GC** to determine the **IMF**. They do mention, however, that even *Gaia* will be unable to detect

* E-mail: wirth@sirrah.troja.mff.cuni.cz (HW)

low-mass stars ($< 0.7M_{\odot}$ for an isochrone and distance of GD-1 and Pal 5) and this does not solve the problem that stars more massive than $\approx 0.8M_{\odot}$ already evolved off the main sequence (Portinari et al. 1998; Marigo 2001), making them undetectable. As Jerabkova et al. (2021) pointed out, the detection of tidal tails is challenging in general. They suggest a new method, the compact convergent point method, to extract the tidal tails.

Kroupa (2001) combined constrains from different studies into what is known as the canonical IMF and concluded that the existing data may be indicating a systematic variation with metallicity. Kroupa (2002) then formulated evidence for the IMF becoming more bottom-light (fewer low mass stars) with decreasing iron abundance. Additionally, Marks et al. (2012) found that the slope of the upper end of the IMF (for stars with a mass $m > 1M_{\odot}$) depends on the initial gas cloud density and the iron abundance. They compared a set of numerical simulations to observations to determine the connection between the initial mass function and the properties of the gas clouds the GCs formed out of. Yan et al. (2021) later found a systematic variation in the low-mass part of the IMF as well.

The purpose of this paper is, thus, to investigate how a varying IMF affects the initial mass computed for the GCs and the number of CCSNe required to reach the observed spread of $[Fe/H]$. The results of this study will be compared to those in Paper I. Sec. 2 explains how the systematic variation of the IMF, as documented in Yan et al. (2021) is applied to the computation of the initial masses of the GCs. Additionally the method to compute the time after which SF ends is explained. Secs. 3 and 4 contain the results and discussion, respectively, and finally we will draw our conclusions in Sec. 5.

2 METHODS

2.1 Cluster initial mass as a function of the IMF

In Paper I the results from Baumgardt & Makino (2003) were used to compute the initial stellar mass of the cluster, M_{ini} . Note that this is the mass after revirialisation following a GC's gas expulsion. Baumgardt & Makino (2003) use the connection between dissolution time, t_{diss} , half-mass relaxation time, t_{rh} , and crossing time, t_{cross} , derived in Baumgardt (2001): $t_{\text{diss}} = kt_{\text{rh}}^x t_{\text{cross}}^{1-x}$. They combine this with the results of their simulations to formulate an equation for the dissolution time of clusters and another one for the evolution of their mass. In Paper I, these findings were combined into one implicit equations that can be solved for M_{ini} numerically:

$$0 = \beta \left[\frac{\frac{M_{\text{ini}}}{\langle m \rangle}}{\ln(\gamma \frac{M_{\text{ini}}}{\langle m \rangle})} \right]^x \frac{R_{\text{ap}}}{\text{kpc}} (1 - e) \frac{1 - \frac{M(t)}{p_{\text{SF}} M_{\text{ini}}}}{\frac{t}{\text{Myr}}} - 1. \quad (1)$$

Note that for consistency the terms are written down in the same order as in Paper I. β and x are fitting parameters which depend on the King concentration parameter, W_0 . $\gamma = 0.02$ is the Coulomb logarithm. R_{ap} and e are the apocentre and eccentricity of the GC's orbit, respectively. $M(t)$ is the current mass of the GC and t its age. Analogous to Paper I, the age is assumed to be 12 Gyr in accordance with literature values (Dotter et al. 2010; Usher et al. 2019; Cohen et al. 2021). The

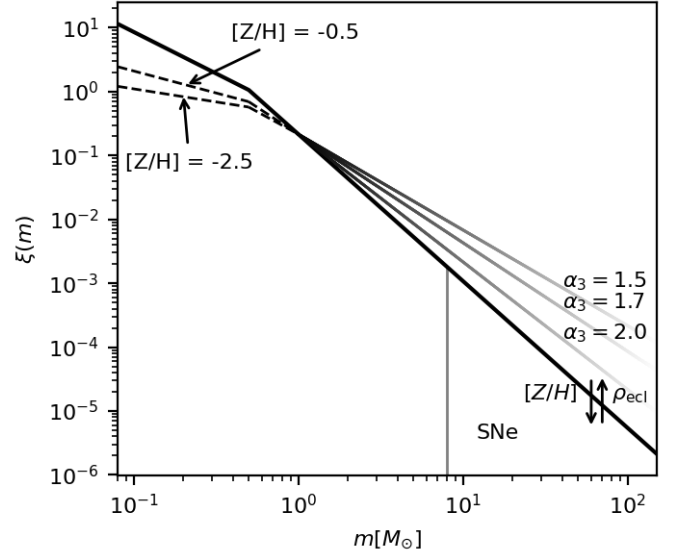


Figure 1. The canonical mass function $\xi(x)$ normalized to one (the area below the curve is the number fraction of stars). The mass beyond which stars are expected to explode in a CCSN ($> 8M_{\odot}$) is marked with a vertical grey line. Additionally, changes to the low-mass part of the mass function depending on $[Z/H]$ (dashed line, Eqs. 2 and 3), and the metallicity- and density-dependent α_3 (faded line, Eqs. 4 to 5) are shown.

mean stellar mass $\langle m \rangle$ and the portion of M_{ini} lost through stellar evolution, p_{SF} , will here be computed depending on the IMF. This is assumed to happen instantaneously (Baumgardt & Makino 2003). Paper I follows Baumgardt & Makino (2003) and assumes $p_{\text{SF}} = 0.7$, which means that 30% of the initial mass was assumed to be lost due to stellar evolution for an invariant canonical IMF.

2.1.1 Dependence of the IMF on initial cluster mass

The IMF, $\xi(m)$, is defined through the number of stars born together in the mass interval $[m, m + dm]$, $dN = \xi(m)dm$. Marks et al. (2012) derived the correlation between the IMF, initial central density and metallicity of a GC by comparing numerical results based on gas-expulsion simulation with observations. Using more recent data, Yan et al. (2021) rewrote the variations in all parts of the IMF as a function of $[Z/H]$ rather than $[Fe/H]$. They formulated the IMF, $\xi(m) = k_i m^{-\alpha_i}$, as:

$$\alpha_1 = 1.3 + \Delta\alpha(10^{[Z/H]_{\text{ini}}} - 1)Z_{\odot}, \quad 0.08 \leq \frac{m}{M_{\odot}} \leq 0.5, \quad (2)$$

$$\alpha_2 = 2.3 + \Delta\alpha(10^{[Z/H]_{\text{ini}}} - 1)Z_{\odot}, \quad 0.5 < \frac{m}{M_{\odot}} \leq 1, \quad (3)$$

$$\alpha_3 = \begin{cases} 2.3, & y < -0.87, \\ -0.41y + 1.94, & y \geq -0.87, \end{cases} \quad 1 < \frac{m}{M_{\odot}}, \quad (4)$$

$$y = -0.14[Z/H]_{\text{ini}} + 0.99 \log_{10}(\rho_{\text{gas}}/(10^6 M_{\odot} \text{pc}^{-3})), \quad (5)$$

with the initial metallicity of the GC, $[Z/H]_{\text{ini}}$, and its cloud core density, ρ_{gas} . $Z_{\odot} = 0.0142$ is the metal mass fraction in

the Sun, $\Delta\alpha = 63$ is a constant and k_i is a constant assuring the function is continuous and normalized.

Following Forbes et al. (2011), $[Fe/H]$ is converted to the total metallicity, $[Z/H]$, using $[Z/H] = [Fe/H] + [\alpha/H]$. The value of $[\alpha/H] = 0.3$ is typical for Galactic GCs (Carney 1996; Forbes et al. 2011). The dependency of the IMF on the metallicity and ρ_{gas} is not arbitrary, but has been extracted from data such that the IMF is consistent with:

- direct observational constraints from the Galactic field population and a large range of star clusters (Kroupa 2002; Marks et al. 2012),
- the observed dynamical mass-to-light ratios and numbers of low-mass X-ray binary systems in ultra-compact dwarf galaxies (Dabringhausen et al. 2009, 2012),
- the synthesised galaxy-wide IMFs of galaxies of different types (Yan et al. 2017), as well as
- galaxy chemical evolution studies (Yan et al. 2021).

All the aforementioned IMF constraints have uncertainties, but the self-consistency-check attained by calculating galaxy-wide stellar populations (Kroupa et al. 1993; Yan et al. 2017; Jeřábková et al. 2018; Yan et al. 2020, 2021) suggests that any true variation is comparable to the above formulation.

Marks & Kroupa (2012) found the following correlation between the density, ρ_{ecl} , and the mass, M_{ecl} , of the stars in the still gas embedded clusters by fitting the densities and masses of several datasets (see their fig. 6):

$$\log_{10} \frac{\rho_{\text{ecl}}}{M_{\odot} \text{pc}^{-3}} = a \log_{10} \frac{M_{\text{ecl}}}{M_{\odot}} + b, \quad (6)$$

with $a = 0.61 \pm 0.13$ and $b = 2.08 \pm 0.69$. The gas density of the cloud is then $\rho_{\text{gas}} = \frac{\rho_{\text{ecl}}}{\epsilon}$, where ϵ is the star formation efficiency (SFE). In agreement with Paper I, $\epsilon = 0.3$ is assumed (see e.g. Lada & Lada 2003; André et al. 2014; Megeath et al. 2016; Banerjee & Kroupa 2018). Based on the gas expulsion computations by Brinkmann et al. (2017) it is assumed that a GC loses a negligible fraction of its stars when its residual gas is expelled, i.e. $M_{\text{ini}} = M_{\text{ecl}}$ to a good approximation. With these calculations, the IMF can now be expressed in dependence of M_{ini} and $[Fe/H]$.

Possible forms of the IMF are illustrated in Fig. 1. The canonical IMF is shown by the thick black line. The changes in α_1 and α_2 depending on $[Fe/H]$ are made visible by dashed lines. Additionally, the shape of the IMF for different α_3 are shown. The IMFs becomes more bottom-light (fewer low mass stars per star formed) with decreasing $[Fe/H]$. Simultaneously, a lower $[Fe/H]$ and a higher gas density ρ_{gas} decrease α_3 , making the GC more top-heavy (more high-mass stars per star formed). We note that this observationally motivated IMF variation (Eqs. 2 to 5) needs to be further tested, but the variation fulfils the observational constraints from resolved stellar populations and the Galactic field as detailed in Kroupa et al. (2013); Jeřábková et al. (2018); Yan et al. (2021). The deduced top-heavy IMF for massive GCs changes the dynamical behaviour of the clusters compared to the canonical IMF (Haghi et al. 2020; Mahani et al. 2021; Wang & Jerabkova 2021).

As in Paper I, the IMF was used to compute the mean

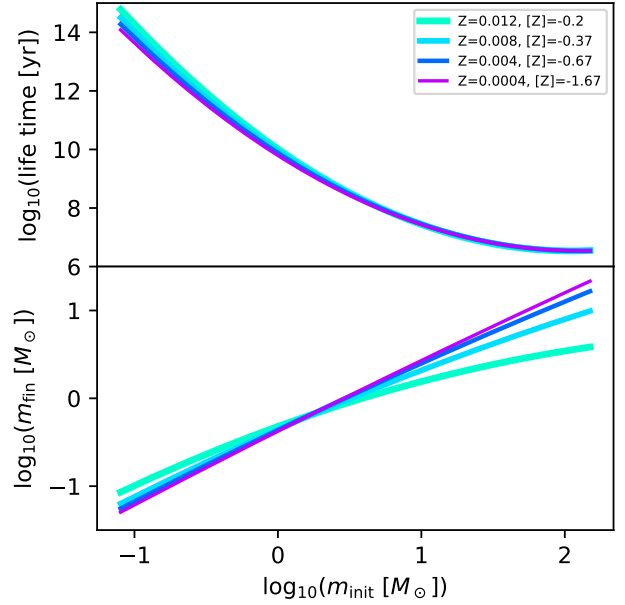


Figure 2. The stellar lifetimes and remnant masses, m_{fin} , of stars as a function of their initial masses, m_{init} , adapted from fig. 3 of Yan et al. (2019).

stellar mass:

$$\langle m \rangle = \frac{\int_{m_{\text{low}}}^{m_{\text{up}}} dm m \xi(m)}{\int_{m_{\text{low}}}^{m_{\text{up}}} dm \xi(m)}, \quad (7)$$

where $m_{\text{low}} = 0.08M_{\odot}$ and m_{up} are the minimum and maximum stellar masses in the GCs, respectively. m_{up} is computed for each GC by solving eqs. 2 - 4 of Yan et al. (2017), replacing the fixed value of $m_{\text{up}} = 120 M_{\odot}$ used in Paper I.

2.1.2 Mass lost through stellar evolution

To compute p_{SF} , the life expectancies and remnant masses for stars given in Fig. 2 are used. These were obtained by Yan et al. (2019) by fitting splines (a function defined piecewise as polynomials) to data provided in Portinari et al. (1998) and Marigo (2001). These authors obtained their data from theoretical models. To find p_{SF} the fraction of the initial mass of a GC that is left depending on its age needs to be computed, neglecting dynamical evolution and thus only focussing on the effects of stellar evolution.

Computing the mass loss of a star over time requires complicated numerical models (Sukhbold et al. 2016; Farrell et al. 2022). However, stars lose most of their mass, after hydrogen burning is over i.e. towards the end of their life (Willson 2000; Heger et al. 2003b). This justifies the simplification used in the present work that all of the mass a star loses is subtracted at the end of its life. It follows then that in a given time interval a GC loses the difference between the initial mass and the remnant mass of all stars dying within this time. The IMF gives us the mass distribution of stars in the GC, with which we can now compute the mass portion of

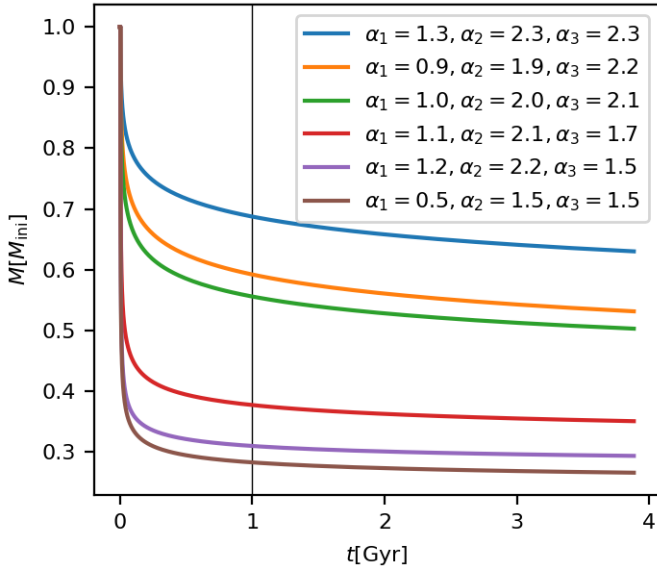


Figure 3. The remaining cluster mass, as mass fraction of the initial mass, taking only stellar evolution into account for different IMFs. $t = 1$ Gyr is marked with the vertical thin black line. The canonical IMF is given by the blue line. The other IMFs assume from top to bottom: $\left(\frac{\rho_{\text{gas}}}{10^6 M_{\odot} \text{pc}^{-3}}, [Z/H]_{\text{ini}}\right) = (0.21, -0.55), (0.38, -0.48), (3.76, -0.41), (11.93, -0.35), (8.83, -1.28)$.

M_{ini} left over in a GC after accounting for stellar evolution at any given time.

Fig. 3 shows the evolution of the GC mass computed as above for various combinations of α_1 , α_2 and α_3 . As we can see, the majority of a GC’s mass loss through stellar evolution happens before the 1 Gyr mark, while the impact made by dynamical evolution is expected to still be small at this point given the long two body relaxation times. This is no hard boundary and one could easily use 0.5 or 1.5 Gyr instead. It is worth noting that core collapse happens quicker for GCs with more top-heavy IMF and for GCs with a higher central density. This might be taken into account in future models (Gürkan et al. 2004). The dominance of the mass loss through stellar evolution is consistent with the findings of Baumgardt & Makino (2003) (see their fig. 1), while Joshi et al. (2001) and Lamers et al. (2010) find slightly higher values for the time for which mass loss through stellar evolution dominates (up to 10 Gyr). However, as Fig. 3 shows, the additional mass loss after 1 Gyr is small. The mass of stars dying at this time is around $2 M_{\odot}$ which classify as cool stars. Therefore, this time is used to estimate p_{SF} .

As mentioned below Eq. 1, the mass loss through stellar evolution is assumed to happen instantaneously at the beginning of GC evolution. This is possible since this mass loss dominates with respect to the dynamical mass loss during the GC’s initial evolution, but plays only a small role afterwards (Baumgardt & Makino 2003). A more detailed numerical study of GCs and their mass loss depending on the IMF can be found in Haghi et al. (2020).

It is worth noting that the mass lost through stellar evolution from the initial population is not added to the remaining gas mass from which the enriched stars form. In the present sample, the mass of the gas returned would have been be-

tween 0.1 and 0.2 M_{ini} for most GCs. The GC experiencing the largest gas return is NGC 6441, which would regain 41 % of its initial mass in gas. This would add up to an extra 18 % more gas to the amount of gas to be polluted in Eq. 15. Therefore, gas return can be neglected.

2.1.3 The parameters β and x

Baumgardt & Makino (2003) fitted β and x to their Nbody results only for clusters with a King concentration parameter $W_0 = 5.0$ and $W_0 = 7.0$ with $x = 0.75, \beta = 1.91$ and $x = 0.82, \beta = 1.03$, respectively. However, in this work, β and x for W_0 between 0.7 and 9 is needed, which is the range of W_0 we find for the GCs in our sample. Therefore, W_0 is computed depending on the initial mass and then extrapolated linearly from the values given above.

To this end the tidal radius, r_t , is calculated as given by eq. 1 of Baumgardt & Makino (2003),

$$r_t = \left(\frac{GM_{\text{ini}}}{2V_G^2}\right)^{\frac{1}{3}} R_p^{\frac{2}{3}}, \quad (8)$$

where G is the Newtonian gravitational constant, V_G is the circular velocity of the Galaxy at the coordinates of the GC and R_p the pericentre distance of the GC. As in Paper I, V_G is assumed to be 220 km s^{-1} . Additionally, the King radius, r_0 , is needed. It is defined in eq. 8.76 of Aarseth et al. (2008),

$$r_0 = \left(\frac{9}{4\pi G} \frac{\sigma^2}{\rho}\right)^{\frac{1}{2}}, \quad (9)$$

with

$$\sigma = \sqrt{\frac{GM_{\text{ini}}}{\epsilon r_h^2}}, \quad \rho = \frac{3M_{\text{ini}}}{8\pi r_h^3}, \quad r_h = 0.10 \text{ pc} \left(\frac{M_{\text{ini}}}{M_{\odot}}\right)^{0.13}.$$

The definition of r_h is taken from Marks & Kroupa (2012). With this the concentration parameter defined as eq. 8.95 in Aarseth et al. (2008) can be computed,

$$c = \log_{10} \left(\frac{r_t}{r_0}\right). \quad (10)$$

Fig. 8.5 of Aarseth et al. (2008) shows the correlation between c and W_0 . Fitting a linear curve going through the graph’s origin to the data using the nonlinear least-squares Marquardt-Levenberg algorithm function (see e.g. Marquardt 1963), the following correlation is obtained:

$$W_0(c) = (4.38 \pm 0.02)c. \quad (11)$$

Interpolating β and x linearly as mentioned at the beginning of this section leads to:

$$\beta = 4.11 - 0.44W_0, \quad (12)$$

$$x = 0.575 + 0.035W_0. \quad (13)$$

With this all quantities required by Eq. 1 can be expressed in terms of M_{ini} . As in Paper I we use the Newton-Raphson method to solve Eq. 1.

2.1.4 The resulting numbers of SNe

The number of CCSNe, N_{SN} , needed to produce the observed iron spread is computed analogous to Paper I:

$$N_{\text{SN}} = \frac{M_{\text{iron}}}{0.074M_{\odot}}, \quad (14)$$

$$M_{\text{iron}} = Z_{\text{Fe},\odot} \left(10^{[Fe/H] + \sigma_{[Fe/H]}} - 10^{[Fe/H] - \sigma_{[Fe/H]}} \right) \times M_{\text{ecl}} \left(\frac{1}{\epsilon} - 1 \right), \quad (15)$$

with the mean iron abundance of the GC, $[Fe/H]$, the iron abundance spread, $\sigma_{[Fe/H]}$, and the fraction of iron in the Sun, $Z_{\text{Fe},\odot} = 0.0013$ (Asplund et al. 2009). The value of $0.074M_{\odot}$ is the average mass of iron released by a CCSN as computed by Maoz & Graur (2017).

2.2 The time after which star formation ends

To compute the time after which SF ends, the equations from Paper I need to be adjusted. Firstly, the IMF needs to be integrated to find the number of expected CCSN, $N_{\text{SN}}^{\text{exp}}$, for each GC separately, instead of having a fixed fraction of the total number of stars as in Paper I:

$$N_{\text{SN}}^{\text{exp}} = \int_{m_{\text{SN}}}^{m_{\text{up}}} dm \xi(m), \quad (16)$$

where $m_{\text{SN}} = 8M_{\odot}$ is the mass above which stars end their lives as CCSNe. As explained in Sec. 2.1.4, N_{SN} of these CCSNe are required to explain the observed iron spread and, therefore, N_{SN} is the number of CCSNe that contribute to SF. The most massive stars are expected to explode first (Fig. 2, Yan et al. 2019). This means that the mass, m_{last} , of the last star to explode in a CCSN which still contributes to SF can be inferred from N_{SN} and $N_{\text{SN}}^{\text{exp}}$:

$$\frac{N_{\text{SN}}}{N_{\text{SN}}^{\text{exp}}} = \frac{\int_{m_{\text{last}}}^{m_{\text{up}}} dm \xi(m)}{\int_{m_{\text{SN}}}^{m_{\text{up}}} dm \xi(m)} = \frac{k_3}{1-\alpha_3} \frac{(m_{\text{up}}^{1-\alpha_3} - m_{\text{last}}^{1-\alpha_3})}{\int_{m_{\text{SN}}}^{m_{\text{up}}} dm \xi(m)}, \quad (17)$$

$$m_{\text{last}} = \left(m_{\text{up}}^{1-\alpha_3} - \frac{N_{\text{SN}}}{N_{\text{SN}}^{\text{exp}}} \frac{1-\alpha_3}{k_3} \int_{m_{\text{SN}}}^{m_{\text{up}}} dm \xi(m) \right)^{\frac{1}{1-\alpha_3}}. \quad (18)$$

Since m_{last} is the mass of a star that explodes as a CCSN, it has to be between the minimum mass from which a star becomes a CCSN, $8M_{\odot}$, and the maximum stellar mass, computed as explained in Sec. 2.1.1. As in Paper I, the expected lifetime for a star with mass m_{last} can be looked up in Fig. 2 for $[Fe/H] = -1.67$, which is close to the $[Fe/H]$ -value of most of the GCs in the present sample (Tab. 1). This lifetime is used as the estimate for the time when further SF ends.

3 RESULTS

The results calculated for a top-heavy IMF are compiled in Tab. 1. As in Paper I the metallicities cited were taken from Bailin (2019) and the present day GC masses and orbital parameters are taken from Hilker et al. (2019). Note that an upgraded catalogue for the metallicities is available (Bailin

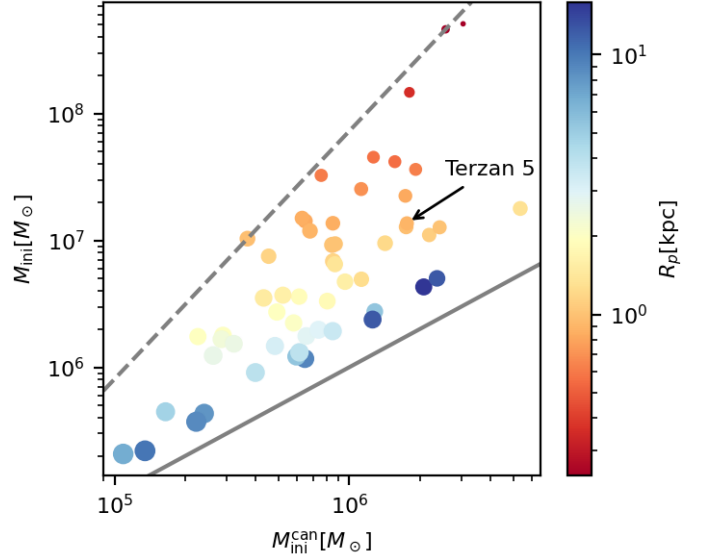


Figure 4. The initial masses computed for the GCs compared to the results from Paper I. The identity function has been marked with a solid grey line and $\frac{M_{\text{ini}}}{M_{\text{ini}}^{\text{can}}} = 1.4 \times 10^{-4} \left(\frac{M_{\text{ini}}^{\text{can}}}{M_{\odot}} \right)^{2.0}$ has been marked with a dashed grey line. The sizes of the dots correlate linearly with α_3 (smaller means a more top-heavy IMF) and the colour indicates the pericentre distance R_p . The cluster Terzan 5 (Sec. 3.1, 3.2) is marked.

& von Klar 2022), however, for consistency with Paper I the old version (Bailin 2019) is used for this work. The data in Table 1 show that the obtained values for the mass function index, α_3 , are all smaller than 2.3 and, therefore, the IMF is more top-heavy than the canonical IMF for all of the GCs. In the following sections the individual properties and how they compare to the results in Paper I will be discussed. The results from Paper I are marked with a superscript ‘can’ (to stand for canonical).

3.1 The initial masses

In Figs. 4 to 8 limiting functions were fitted to the data. The method for obtaining these functions is described in Appendix A. The code to fit these functions can be found on the authors’ github repository¹.

In Fig. 4 the new results computed using a variable IMF, M_{ini} , are compared with the $M_{\text{ini}}^{\text{can}}$ computed using the canonical IMF (Paper I). The differences between M_{ini} and $M_{\text{ini}}^{\text{can}}$ sensitively depend on the assumed IMF variation law, that is, Eqs. 2 to 5. For small α_3 the increase of M_{ini} compared to $M_{\text{ini}}^{\text{can}}$ is larger. That means that GCs with more top-heavy IMFs loose mass more rapidly than GCs with larger α_3 . This is in agreement with Baumgardt et al. (2019)². However, while Baumgardt et al. (2019) conclude that the combined mass of all early GCs in the Galaxy must have been some $10^8 M_{\odot}$, according to the present study calculations the 55

¹ <https://github.com/Henri-astro/LimiFun>

² Note that in Baumgardt et al. (2019) the IMF power-law indices, α_i , are defined with the opposite sign.

Table 1. The observed properties and deduced numbers of CCSNe and times when SF ends for 55 Galactic GCs. The columns from left to right are: the name of the GC, the current mass, $M(t)$, with $t = 12$ Gyr, the pericentre of the GC's orbit, R_p , the apocentre of the GC's orbit, R_{ap} , the computed value for α_3 , initial mass, M_{ini} , iron abundance, $[Fe/H]$, iron abundance spread, $\sigma_{[Fe/H]}$, number of CCSNe, N_{SN} , the number of CCSNe per unit mass, n_{SN} , the expected number of CCSNe to occur in the GC, N_{SN}^{exp} , and the time SF ends, t_{end}^{SF} .

Name	$M(t)$ [$10^5 M_\odot$]	R_p [kpc]	R_{ap} [kpc]	α_3	M_{ini} [$10^5 M_\odot$]	$[Fe/H]$	$\sigma_{[Fe/H]}$	N_{SN}	n_{SN} [M_\odot^{-1}]	N_{SN}^{exp}	t_{end}^{SF} [Myr]
47 Tuc	8.07	5.47	7.44	1.75	27.50	-0.747	0.033	3.25×10^3	1.18×10^{-3}	6.41×10^4	3.5
NGC 288	0.98	2.01	12.26	1.83	17.79	-1.226	0.037	7.82×10^2	4.39×10^{-4}	4.06×10^4	3.4
NGC 362	3.36	1.02	12.41	1.65	93.75	-1.213	0.074	8.52×10^3	9.09×10^{-4}	2.30×10^5	3.5
NGC 1851	2.81	0.85	19.20	1.61	136.44	-1.157	0.046	8.74×10^3	6.41×10^{-4}	3.38×10^5	3.4
NGC 1904	1.56	0.82	19.51	1.62	142.09	-1.550	0.027	2.16×10^3	1.52×10^{-4}	3.52×10^5	3.5
NGC 2419	14.30	15.89	92.20	1.78	42.97	-2.095	0.032	2.21×10^2	5.14×10^{-5}	1.01×10^5	3.5
NGC 2808	8.69	0.97	14.76	1.61	127.73	-1.120	0.035	6.77×10^3	5.30×10^{-4}	3.16×10^5	3.4
NGC 3201	1.41	8.20	24.15	2.00	4.32	-1.496	0.044	1.21×10^2	2.81×10^{-4}	8.75×10^3	3.4
NGC 4590	1.32	8.95	29.51	2.06	3.72	-2.255	0.053	2.19×10^1	5.89×10^{-5}	7.15×10^3	3.4
NGC 4833	1.80	0.90	7.68	1.67	118.88	-2.070	0.013	2.63×10^2	2.21×10^{-5}	2.91×10^5	3.5
NGC 5024	4.17	9.11	22.21	1.92	11.69	-1.995	0.071	1.68×10^2	1.44×10^{-4}	2.53×10^4	3.4
NGC 5053	0.73	10.33	17.74	2.12	2.20	-2.450	0.041	6.38×10^0	2.91×10^{-5}	3.93×10^3	3.4
NGC 5139	33.40	1.33	6.99	1.62	178.36	-1.647	0.271	2.32×10^4	1.30×10^{-3}	4.43×10^5	3.5
NGC 5272	3.60	5.44	15.16	1.88	12.17	-1.391	0.097	9.66×10^2	7.93×10^{-4}	2.69×10^4	3.5
NGC 5286	3.59	1.17	13.32	1.72	68.41	-1.727	0.103	2.66×10^3	3.89×10^{-4}	1.65×10^5	3.4
NGC 5466	0.55	6.80	53.55	2.10	2.07	-1.865	0.075	4.26×10^1	2.05×10^{-4}	3.81×10^3	3.4
NGC 5634	2.20	3.97	23.76	1.94	9.09	-1.869	0.081	20×10^2	2.20×10^{-4}	1.94×10^4	3.4
NGC 5694	3.67	3.90	65.74	1.91	13.10	-2.017	0.046	1.16×10^2	8.84×10^{-5}	2.86×10^4	3.4
NGC 5824	8.49	12.48	33.72	1.85	23.77	-2.174	0.058	1.85×10^2	7.78×10^{-5}	5.38×10^4	3.5
NGC 5904	3.68	2.89	24.03	1.83	17.63	-1.259	0.041	7.96×10^2	4.51×10^{-4}	4.02×10^4	3.4
NGC 5986	3.31	0.70	5.08	1.56	253.81	-1.527	0.061	9.21×10^3	3.63×10^{-4}	6.34×10^5	3.4
NGC 6093	2.64	0.36	3.53	1.38	1467.87	-1.789	0.014	6.67×10^3	4.54×10^{-5}	3.67×10^6	3.5
NGC 6121	0.93	0.62	6.20	1.51	325.37	-1.166	0.050	2.22×10^4	6.82×10^{-4}	8.14×10^5	3.4
NGC 6139	3.48	1.37	3.58	1.71	64.92	-1.593	0.033	1.09×10^3	1.68×10^{-4}	1.57×10^5	3.4
NGC 6171	0.81	1.16	3.74	1.66	75.02	-0.949	0.047	7.93×10^3	1.06×10^{-3}	1.83×10^5	3.5
NGC 6205	4.69	1.56	8.32	1.74	47.26	-1.443	0.101	3.47×10^3	7.33×10^{-4}	1.13×10^5	3.4
NGC 6218	0.87	2.37	4.80	1.84	16.64	-1.315	0.029	4.66×10^2	2.80×10^{-4}	3.77×10^4	3.4
NGC 6229	2.88	2.05	30.94	1.80	22.35	-1.129	0.044	1.46×10^3	6.54×10^{-4}	5.17×10^4	3.5
NGC 6254	1.89	1.98	4.59	1.80	27.25	-1.559	0.049	7.37×10^2	2.71×10^{-4}	6.33×10^4	3.4
NGC 6266	6.90	0.83	2.36	1.55	224.31	-1.075	0.041	1.55×10^4	6.89×10^{-4}	5.59×10^5	3.4
NGC 6273	6.57	1.22	3.34	1.68	95.00	-1.612	0.161	7.63×10^3	8.03×10^{-4}	2.32×10^5	3.4
NGC 6341	3.12	1.00	10.57	1.71	92.11	-2.239	0.083	8.85×10^2	9.61×10^{-5}	2.23×10^5	3.5
NGC 6362	1.16	2.54	5.16	1.84	15.32	-1.092	0.017	4.21×10^2	2.75×10^{-4}	3.47×10^4	3.4
NGC 6366	0.43	1.97	5.31	1.79	17.45	-0.555	0.071	6.92×10^3	3.97×10^{-3}	3.93×10^4	4.9
NGC 6388	11.30	1.11	3.78	1.59	110.26	-0.428	0.054	4.45×10^4	4.03×10^{-3}	2.66×10^5	4.2
NGC 6397	0.90	2.63	6.23	1.91	12.37	-1.994	0.028	7.02×10^1	5.67×10^{-5}	2.69×10^4	3.5
NGC 6402	7.39	0.63	4.36	1.50	362.45	-1.130	0.053	2.85×10^4	7.86×10^{-4}	9.07×10^5	3.4
NGC 6441	12.50	1.00	3.91	1.57	126.76	-0.334	0.079	9.31×10^4	7.35×10^{-3}	3.04×10^5	5.9
NGC 6535	0.13	0.97	4.50	1.68	103.20	-1.963	0.035	7.86×10^2	7.61×10^{-5}	2.52×10^5	3.5
NGC 6553	4.45	1.26	2.32	1.66	49.39	-0.151	0.047	3.28×10^4	6.64×10^{-3}	1.08×10^5	6.3
NGC 6569	2.28	1.88	2.97	1.73	36.03	-0.867	0.055	5.39×10^3	1.49×10^{-3}	8.54×10^4	3.6
NGC 6626	2.84	0.58	2.89	1.49	452.45	-1.287	0.075	3.51×10^4	7.77×10^{-4}	1.13×10^6	3.4
NGC 6656	4.09	2.95	9.48	1.86	19.75	-1.803	0.132	8.31×10^2	4.21×10^{-4}	4.46×10^4	3.4
NGC 6681	1.20	0.85	4.93	1.62	149.57	-1.633	0.028	1.95×10^3	1.30×10^{-4}	3.70×10^5	3.5
NGC 6715	16.20	12.50	36.59	1.74	50.19	-1.559	0.183	5.21×10^3	1.04×10^{-3}	1.20×10^5	3.5
NGC 6752	2.32	3.23	5.37	1.87	14.72	-1.583	0.034	2.61×10^2	1.77×10^{-4}	3.29×10^4	3.4
NGC 6809	1.88	1.59	5.54	1.79	36.99	-1.934	0.045	3.87×10^2	1.05×10^{-4}	8.66×10^4	3.5
NGC 6838	0.63	4.75	7.08	1.95	4.46	-0.736	0.039	6.38×10^2	1.43×10^{-3}	9.11×10^3	3.8
NGC 6864	4.10	1.80	17.51	1.76	33.22	-1.164	0.059	2.69×10^3	8.10×10^{-4}	7.84×10^4	3.5
NGC 7078	4.99	3.57	10.40	1.88	19.26	-2.287	0.053	1.05×10^2	5.48×10^{-5}	4.28×10^4	3.5
NGC 7089	5.20	0.56	16.93	1.50	417.15	-1.399	0.021	6.98×10^3	1.67×10^{-4}	1.05×10^6	3.5
NGC 7099	1.39	1.49	8.17	1.82	35.18	-2.356	0.037	1.15×10^2	3.26×10^{-5}	8.12×10^4	3.5
Terzan 1	2.72	0.24	1.48	1.22	5089.44	-1.263	0.037	2.05×10^5	4.03×10^{-4}	1.23×10^7	3.4
Terzan 5	7.60	0.89	2.96	1.56	136.44	-0.092	0.295	7.01×10^5	5.14×10^{-2}	3.27×10^5	-
Terzan 8	0.58	0.24	1.65	1.29	4604.79	-2.255	0.098	5.05×10^4	1.10×10^{-4}	1.13×10^7	3.5

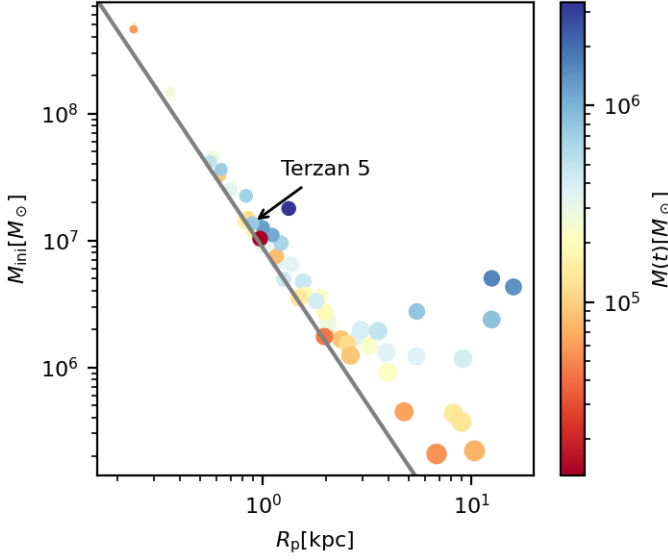


Figure 5. The initial masses computed for the GCs in dependence of the pericentre distance. Eq. 19 has been marked with a grey line. The sizes of the dots correlate linearly with α_3 (smaller means a more top-heavy IMF) and the colour indicates the present-day mass $M(t)$. The cluster Terzan 5 (Sec. 3.1, 3.2) is marked.

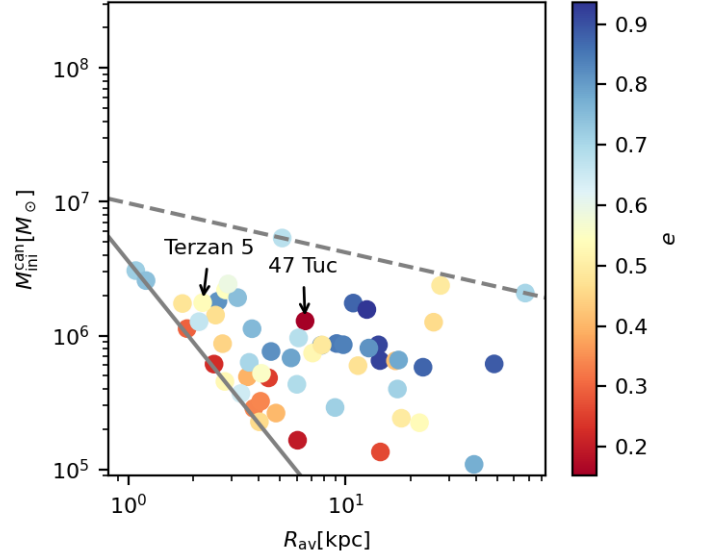


Figure 7. The same as Fig. 6 but the initial masses are computed using the canonical IMF. The function $\frac{M_{\text{ini}}^{\text{can}}}{M_{\odot}} = 3.6 \times 10^6 \left(\frac{R_{\text{av}}}{\text{kpc}}\right)^{-2.0}$ has been marked with a solid grey line and $\frac{M_{\text{ini}}^{\text{can}}}{M_{\odot}} = 9.8 \times 10^6 \left(\frac{R_{\text{av}}}{\text{kpc}}\right)^{-0.37}$ has been marked with a dashed grey line.

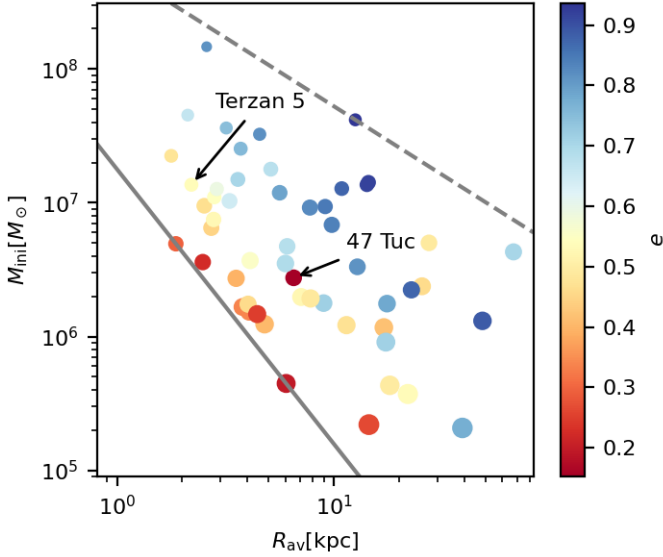


Figure 6. The initial masses computed for the GCs in dependence of the mean orbital distance R_{av} . The function $\frac{M_{\text{ini}}}{M_{\odot}} = 1.8 \times 10^7 \left(\frac{R_{\text{av}}}{\text{kpc}}\right)^{-2.1}$ has been marked with a solid grey line and $\frac{M_{\text{ini}}}{M_{\odot}} = 5.6 \times 10^8 \left(\frac{R_{\text{av}}}{\text{kpc}}\right)^{-1.0}$ has been marked with a dashed grey line. The sizes of the dots correlate linearly with α_3 (smaller means a more top-heavy IMF) and the colour indicates the orbital eccentricity e . The clusters Terzan 5 (Sec. 3.1, 3.2) and 47 Tuc (Sec. 4.2) are marked.

GCs in our sample already exceed this mass. Part of the reason is the higher maximum stellar mass in this work. Baumgardt et al. (2019) used only $m_{\text{up}} = 15M_{\odot}$ for all of their GCs, while in this study the $M_{\text{ecl}}-m_{\text{up}}$ -relation found by Yan et al. (2017) is used. With this, values for m_{up} between 140 and $150 M_{\odot}$ are found for the GCs studied here. Consequently, in the most massive GCs studied here up to 80 % of the initial mass is in stars more massive than $15M_{\odot}$.

Another question the top-heavy IMF leads to is, how many stars can form in a GC before star formation is suppressed due to the heating of the gas. Several studies showed that stellar winds and radiation can disperse the gas in a stellar cluster before the first CCSNe occur (Lada & Lada 2003; Dale et al. 2012; Verliat et al. 2022). The overabundance of massive stars relative to the canonical IMF would increase these effects and could eventually prevent iron-enhanced stars from forming. However, further investigation is required to estimate the exact magnitude of these effects depending on the IMF and the birth gas density, ρ_{gas} and $[Fe/H]$.

As expected from Eqs. 4 and 6 and visible in Fig. 4, M_{ini} increases with decreasing α_3 . Since α_3 is below the value for the canonical IMF for all GCs, M_{ini} is always larger than $M_{\text{ini}}^{\text{can}}$. The difference between M_{ini} and $M_{\text{ini}}^{\text{can}}$ increases with decreasing R_{p} . This is partly because the tidal radius computed using Eq. 8 is the tidal radius of the GC at its pericentre. This means that the mass loss for low- R_{p} -GCs is stronger, which means that their initial masses were larger and therefore their α_3 is increased. A similar but weaker correlation can be found, if a similar plot is done with R_{ap} , as defined below Eq. 1, instead of R_{p} . This leads to the conclusion that the difference between M_{ini} based on a top-heavy IMF compared to $M_{\text{ini}}^{\text{can}}$ based on a canonical IMF is larger for GCs closer to the Galactic centre.

The smaller R_p is for a GC, the stronger is the tidal force from the Galactic gravitational field it is exposed to. This means that the dissolution times for GCs get smaller with decreasing R_p . Therefore, if a GC comes close enough to the Galactic centre, its dissolution time becomes smaller than the age of the present day GCs, 12 Gyr (Dotter et al. 2010; Usher et al. 2019; Cohen et al. 2021). As visible in Figs. 4 and 5, there is a lack of low- R_p -GCs at the lower end of M_{ini} . The lower limit for not yet dissolved GCs is found at:

$$\frac{M_{\text{ini}}}{M_{\odot}} = 8.7 \times 10^6 \left(\frac{R_p}{\text{kpc}} \right)^{-2.5}. \quad (19)$$

That this is the lower limit for undissolved GCs is further supported by the fact that the present-day masses of the GCs get smaller for GCs closer to the boundary. It is, however, likely for these GCs to still exist as dark clusters to this day (Banerjee & Kroupa 2011). Furthermore, there appears to be a lack of distant initially massive GCs. This is even more visible in Fig. 6, which shows M_{ini} over the mean orbital distance over time, $R_{\text{av}} = \frac{R_{\text{ap}} + R_p}{2} \left(1 + \frac{e^2}{2} \right)$ (Stein 1977). This would suggest that more massive GCs formed preferably near the Galactic centre (small R_{av}). In Fig. 7 it is shown that this result holds even if the canonical IMF is used, which indicates that this result is robust.

It is important to note that in both this work and in Baumgardt & Makino (2003), R_p was used to compute the tidal radius (see Sec. 2.1.3). R_p is the smallest distance the GC can have from the Galactic centre. This leads to an underestimate of the tidal radius and therefore an overestimate of the mass loss of a GC. This overestimation is larger for larger eccentricities, since the orbit of a GC with large eccentricity deviates more from a circular orbit with radius R_p . As visible in Fig. 6 the GCs close to the lower boundary (lower grey line) all have very low eccentricities, therefore, the M_{ini} values are expected to be close to the real ones. However, the GCs close to the upper boundary (upper grey line) all have high eccentricities, indicating that we are likely to have overestimated their masses. To determine the actual extent of this overestimate, the simulations of Baumgardt & Makino (2003) would have to be rerun with more precise estimates of the tidal radius. 47 Tuc is an outlier when it comes to the eccentricity and has been labelled in both Figs. 6 and 7.

3.2 The number of SNe and the time SF ends

One of the key results of Paper I was that the number of CC-SNe per unit mass required to reproduce the observed metal-enrichment, n_{SN} , is independent of M_{ini} . Therefore, n_{SN} does not change between this work and Paper I (compare Tab. 1 and tab. 1 in Paper I). However, the change in M_{ini} propagates through to N_{SN} in the form $N_{\text{SN}} = n_{\text{SN}} M_{\text{ini}}$. This leads to the behaviour visible in Fig. 8, which is similar to that for M_{ini} in Fig. 4. The difference between N_{SN} and $N_{\text{SN}}^{\text{can}}$ is larger for GCs closer to the Galactic centre.

As in Paper I, the number of CCSNe required to produce the iron spread observed in Terzan 5 is larger than $N_{\text{SN}}^{\text{exp}}$. This leads to the conclusion that Terzan 5 must have been formed through a different scenario, like for example a merger (Massari et al. 2014, Paper I). GCs with unusual chemical compositions can also form through the merger of two chem-

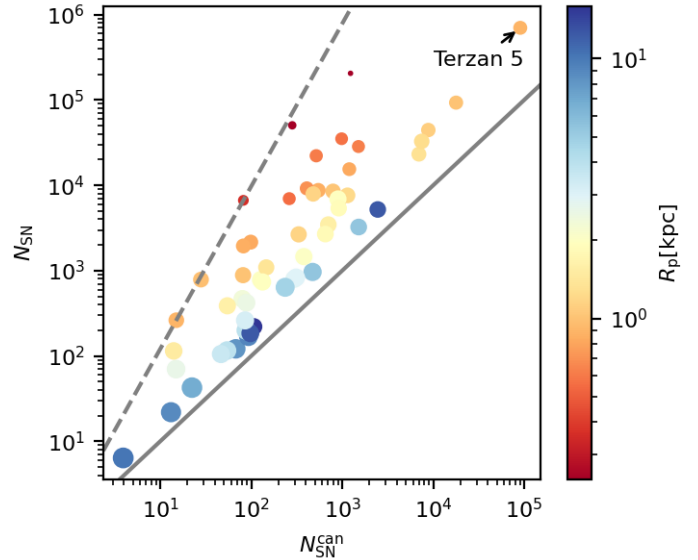


Figure 8. The required numbers of SN computed for the GCs compared to the results from Paper I. The identity function has been marked with a solid grey line and $N_{\text{SN}} = 1.5 (N_{\text{SN}}^{\text{can}})^{1.9}$ has been marked with a dashed grey line. The size of the dots correlates linearly with α_3 (smaller means a more top-heavy IMF) and the colour indicates the Galactocentric pericentre distance. The cluster Terzan 5 (Sec. 3.1, 3.2) is marked.

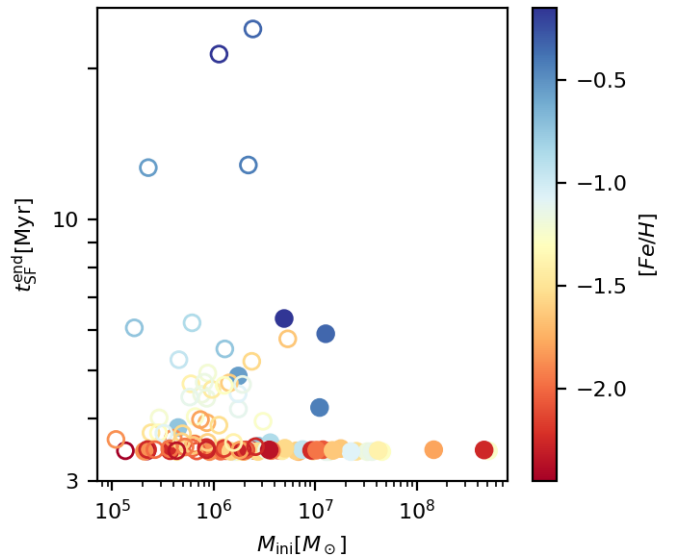


Figure 9. The time until SF ends. The empty circles are the datapoints computed using the canonical IMF from Paper I, the filled ones are from this work. The colour indicates the iron abundance.

ically distinct molecular clouds (Han et al. 2022). Terzan 5 has been marked in all relevant figures.

In Fig. 9 the time when SF ends is plotted over M_{ini} and compared to our data from Paper I. Note that Terzan 5 is missing, since the required number of CCSNe exceeds the number of CCSNe expected for this GC (see Tab. 1). This makes it impossible to compute t_{SF} . The calculated times un-

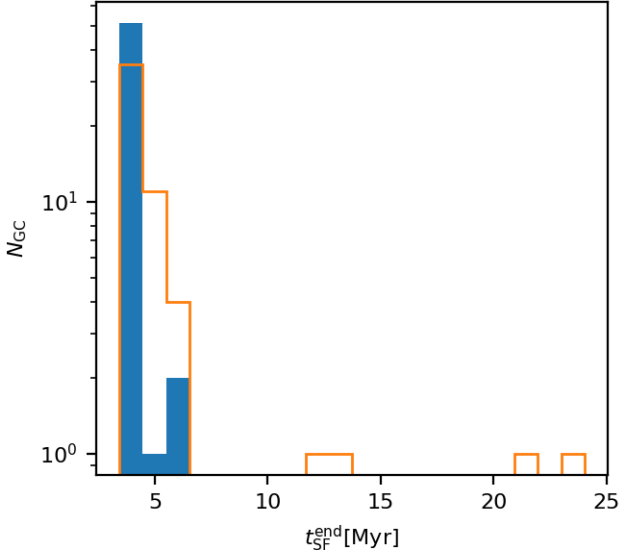


Figure 10. Distribution of the times, $t_{\text{SF}}^{\text{end}}$, when star formation ends for the clusters in our sample. N_{GC} stands for the number of clusters in a given bin. The blue bars show the data computed in the present work, the orange bars show the data computed using a canonical IMF in Paper I. Note that the values of $t_{\text{SF}}^{\text{end}}$ have a smaller dispersion for the variable IMF.

til SF ends depend on the assumed lifetime of massive stars (Fig. 2). Different stellar evolution models can result in different lifetimes with uncertainties of a few Myr. The increase of M_{ini} discussed in Sec. 3.1 is clearly visible in this plot. Additionally, the time until SF ends is reduced significantly. This is because GCs with top-heavy IMFs produce a larger fraction of their CCSNe early on due to the larger fraction of massive stars. The times until SF ends obtained here are in agreement with the times after which GCs have been observed to be free of gas (Bastian & Strader 2014) and with theoretical models concerning the timescales with which gas is expelled from GCs via CCSNe (Calura et al. 2015).

Similar to Fig. 9, Fig. 10 shows the time until SF ends, however, this time in the form of a histogram. It is clearly visible that $t_{\text{SF}}^{\text{end}}$ is shorter using a top-heavy IMF compared to the results of our calculations using a canonical one. For most GCs, SF ends after 3.5 – 4 Myr. As for the results computed with the canonical IMF, this is in agreement with studies showing that the GCs and young massive clusters are gas free after at most 10 Myr (Calura et al. 2015; Krause et al. 2016).

The correlation between the mean iron abundance and the time until SF ends observed in Paper I is also apparent in our data (Fig. 9) with a variable IMF. However, as in Paper I, this might be due to an underestimate of the error of the iron spread, which would increase the calculated number of CCSNe preferentially for GCs with large mean iron abundances. Therefore, it is unclear whether or not this is a physical effect. According to Marks et al. (2012), a higher mean iron abundance is expected to lead to a less top-heavy IMF. Therefore, the portion of massive stars would be lower, which would lead to fewer CCSNe early on in GC evolution. This means that it is expected that gas is driven out more slowly leading to

a larger $t_{\text{SF}}^{\text{end}}$, which would support the result we observe in Fig. 9.

4 DISCUSSION

4.1 The upper mass limit of GCs

As stated in Sec. 3.1, the upper initial mass limit of GCs decreases with increasing distance from the Galactic centre. The same has been observed by Pflamm-Altenburg et al. (2013) for young star clusters around M33. They suggested that this would be due to higher gas surface densities (more material) in the inner regions of galaxies.

The star clusters in M33 are very young (≤ 10 Myr, Sharma et al. 2011; Pflamm-Altenburg et al. 2013) and, therefore, the mass loss experienced by these clusters is expected to be small ($M_{\text{cl}} \approx M_{\text{ini}}$, with the current cluster mass M_{cl}). Pflamm-Altenburg et al. (2013) expressed the mass of the most massive clusters in their radially binned sample as a function of their current galactocentric distance, R , using the following expression:

$$\log_{10} \left(\frac{M_{\text{cl}}}{M_{\odot}} \right) = a \frac{R}{\text{kpc}} + b. \quad (20)$$

By fitting this function to the data from the clusters in M33, they found that the clusters with the highest mass roughly followed the function with $a = -1.7 \times 10^{-4}$ and $b = 4.67$. To obtain their fit they distributed their clusters into bins of 17 clusters each depending on their radial distance to the centre of M33. They then used the $\frac{R}{\text{kpc}}$ - and $\log_{10} \left(\frac{M_{\text{cl}}}{M_{\odot}} \right)$ -values of the most massive clusters in each bin to obtain their fit. In this work, the maximum GC mass is fitted using the method explained in App. A and which lead to $\log_{10} \left(\frac{M_{\text{ini}}}{M_{\odot}} \right) = 8.7 - \log_{10} \left(\frac{R_{\text{av}}}{\text{kpc}} \right)$ as the upper boundary (see Fig. 6). This means that the upper limits of the initial masses of the GCs in our Galaxy are about three orders of magnitude higher than the ones in M33. Note, however, that in both cases the sample size is too small to reliably determine the shape of the radial upper limit function.

While both, M33 and the very young Galaxy have their newly-formed, most massive cluster masses decrease systematically with the galactocentric radius, the two cases are very different: M33 is a late-type disk galaxy about ten times less massive than the Galaxy (Corbelli 2003; McMillan 2011; Kafre et al. 2012; McMillan 2017), is on the galaxy main sequence and is forming open star clusters, while the GC system studied here consists of 12 Gyr old GCs in the Galactic halo. Since the mean GC mass increases with the mass of the host galaxy (Harris et al. 2013) we expect differences in the maximum mass function for those two systems.

4.2 Consequences for the Galaxy

Assuming the Galaxy and all GCs were also formed in-situ (Gilmore & Wyse 1998), eqs. 9 - 12 from Yan et al. (2017) can be used to compute the star formation rate (SFR) of the Galaxy at the time the GCs were forming. With a maximum GC mass of $5.1 \times 10^8 M_{\odot}$ for Terzan 1 we compute a SFR of $351 M_{\odot}/\text{yr}$. This is about 100 times higher than the

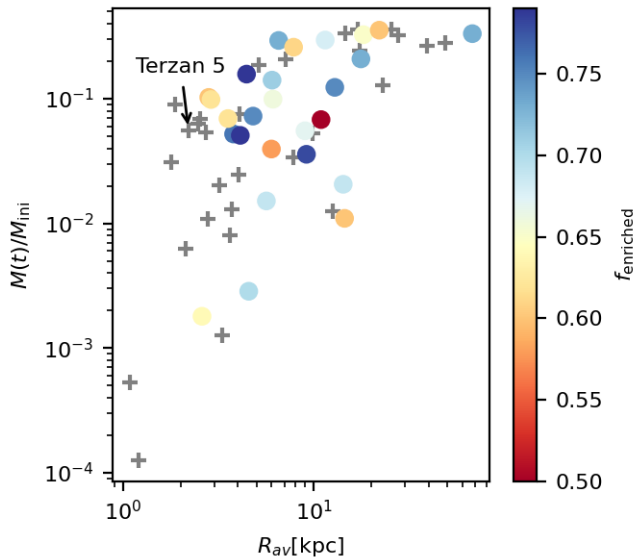


Figure 11. The fraction of mass left over in a GC at the current time over its Galactocentric distance. The GCs are colour-coded for the fraction of the enriched population within them. Those GCs for which the fraction of the enriched population is not known are marked with a ‘+’. The cluster Terzan 5 (Sec. 3.1, 3.2) is marked.

mean SFR of the Galaxy and could be due to SFR fluctuations, or due to the most massive GCs having a different origin. It is, however, worth mentioning that especially for massive GCs, like ω Cen and Terzan 5, alternative formation scenarios, such as mergers or being the remnant of a tidally thrashed dwarf galaxy, have been proposed (see e.g. Bekki & Freeman 2003; Massari et al. 2014; Marks et al. 2022). If the real maximum GC mass was, for example, only half as large, the SFR becomes $132M_{\odot}/\text{yr}$. If the three most massive GCs ($> 10^8 M_{\odot}$) of the sample are excluded, less than a tenth of the maximum GC mass used above is needed. The resulting SFR is only $1M_{\odot}/\text{yr}$.

As visible in Fig 11 the closer a GC is to the Galactic centre, the larger the mass fraction it lost with respect to its initial mass. This is a direct consequence of the results of the numerical experiments by Baumgardt & Makino (2003). Contrary to this, Bastian & Lardo (2015) concluded, based on a lack of a connection between the radial distance of a GC to the Galactic centre and the fraction of enriched stars within it, that no radial dependency between the cluster mass loss and its coordinates exists. They expect a radial dependency to exist due to a preferential loss of 1st generation stars which are known to be less concentrated. In a stronger tidal field they should, therefore, be lost faster and their present day fraction in the GC should be lower. Bastian & Lardo (2015) define first-generation stars as those with sodium abundance, $[Na/Fe]$, between $[Na/Fe]_{\min}$ and $[Na/Fe]_{\min} + 0.3$. The minimum sodium abundance, $[Na/Fe]_{\min}$, of a GC was determined by eye from $[O/Fe]$ - $[Na/Fe]$ -plots of the GCs excluding outlying stars. However, Marino et al. (2019) find that in many GCs the difference between first and second generation is smaller than this. In fact, the $[Na/Fe]$ -values of 1st and second generation stars overlap in some of the cases.

Bastian & Lardo (2015) used present-day fractions of en-

riched stars from a number of studies (Carretta et al. 2009a, 2011, 2012, 2013; Kacharov et al. 2013; Carretta et al. 2014, 2015; Marino et al. 2015). Fig. 11 is colour-coded according to the data collected by Bastian & Lardo (2015). This figure confirms that there is indeed no obvious correlation between the fraction of enriched stars, f_{enriched} , and the GC’s distance from the Galactic centre or the mass fraction remaining. However, due to the large number of datasets used, the unreliable boundary between different generations and the large scatter, this is not conclusive evidence against a preferential mass loss nearer to the Galactic centre.

The higher initial masses of the GCs would imply that a larger portion of the stars in the Galactic halo originated from GCs. The mass of the stellar halo is currently estimated to be up to $1.4 \pm 0.4 \times 10^9 M_{\odot}$ (Deason et al. 2019). Note, however, that this estimate was made using the canonical IMF from *Gaia* measurements of red giants in the halo. A top-heavy galaxy-wide IMF would increase the initial halo mass significantly. Additionally, the number of stellar remnants would be increased (Yan et al. 2021). These remnants would either stay inside the GC or be expelled due to dynamical processes, remaining as free-floating in the halo (Baumgardt et al. 2008). In our sample the number of neutron stars and black holes is on average 36 times higher than when assuming a canonical IMF for all GCs. The most extreme case in this study, Terzan 8, produces 403 times as many neutron stars and black holes as it would with a canonical IMF.

4.3 Improvements for future models

Since a modified version of the method applied in Paper I is used, most of the limitations discussed in sec. 4.2 of Paper I apply in this work as well. Among them is the possibility of failed CCSNe (Pejcha & Thompson 2015; Sukhbold et al. 2016; Basinger et al. 2020; Neustadt et al. 2021), in which case some massive stars would end their lives without contributing any iron. This would lead to longer timespans until SF ends, which is also discussed in Renzini et al. (2022).

The dependence of the iron output on the CCSN mass was also neglected. However, it is likely, that the amount of ejected iron does depend on the mass of the progenitor. From the short timespan after which SF ends (Fig. 9), it follows that only the most massive stars contribute to the iron available for the formation of further stars. Therefore, if for example, the most massive stars would contribute twice as much iron as the average CCSN, only half as many CCSNe would be required and the time until SF ends would become shorter. Calculations by Nomoto et al. (2013) show that, for example, a $40M_{\odot}$ -star with an initial metallicity of $[Z/H] = -1.7$ alone can produce $\approx 0.3M_{\odot}$ in iron. An important upgrade for our model in the future would therefore be to use more detailed CCSNe yield models to more accurately compute the number of CCSNe needed to explain the observed iron spreads. Additionally, supernovae 1a can happen early as edge-lit type 1a SNe (Regős et al. 2003). This has also been neglected.

As shown in Paper I possible errors in measurements of $[Fe/H]$ have a significant influence on the result. In appendix A of Paper I it is shown that an overestimate of the measurement errors for individual stars in the sample by 0.13 dex can lead to an overestimate of the CCSNe required by over 1 dex. Similarly, errors in the mean $[Fe/H]$ for a GC, which

might occur as a result of over- or underestimating the sizes of the different stellar populations within the GCs, can lead to over and underestimates in the number of CCSNe required to explain the iron spread. Since the iron spread is given in dex, its value in absolute numbers depends on the value of $[Fe/H]$ (see Eq. 15). An underestimate of $[Fe/H]$ would lead to an underestimate of the number of CCSNe required and vice versa. For example an underestimate of $[Fe/H]$ by 0.1 would lead to a 20% underestimate of the number of CCSNe required.

One of the main assumptions of our model, not discussed thus far, is that the GCs move on constant Keplerian orbits. However, various effects like encounters with other GCs, gas clouds and dynamical friction could have altered the orbits of the GCs. If the GCs used to be further away then mass loss would also be reduced, which means that we have overestimated M_{ini} . The orbital evolution of GCs could be determined by ‘backwards-integrating’ the paths of all GCs in the Galaxy as in Portegies Zwart & Boekholt (2018), though this would not cover interactions with GCs or molecular clouds that are already dissolved or unknown. The model of Baumgardt & Makino (2003) would have to be expanded to integrate over the orbital path rather than assuming a constant orbit.

Furthermore, a constant SFE of 0.3 is assumed for each GC. In the current model a higher (lower) SFE would lead to a lower (higher) fraction of the gas being left over, which means that less (more) iron was needed to be produced. For a constant gas cloud mass before SF, the mass of iron required, M_{iron} , is proportional to $1 - \epsilon$. Because of this, N_{SN} would increase for a smaller SFE. While the value of the SFE is still unclear, Ashman & Zepf (2001) suggested that the SFE might vary with the density of the molecular cloud the GC forms out of. From Eq. 4 we see that a higher density leads to a more top-heavy IMF, which would lead to more CCSNe expected to explode early on, ensuring a self-regulation of the formation of a GC.

Another pressing question to answer, is how to form new stars in a gas cloud already densely populated by stars, that heat the gas. Parmentier et al. (1999) suggested that the second generation of stars would form in the shock waves caused by CCSNe. This would be in agreement with the present findings, however, it would also mean that the assumption of well-mixed gas in our model would need to be revisited.

5 CONCLUSIONS

In this work the initial masses and numbers of CCSNe required to explain the iron abundance spreads of 55 Galactic GCs is investigated. Based on the assumption that the gas cloud a GC forms out of is well mixed (has the same mean iron abundance at every point in space) and that it is polluted by CCSNe instantaneously, an analytical model is used. The stars are assumed to form with the systematically variable IMF in accordance with Yan et al. (2021), while the initial masses of the GCs are deduced considering stellar evolution as well as the dynamical mass loss of the star clusters, using the algorithm described in Baumgardt & Makino (2003).

The main results of this work summarize as follows:

(1) The initial masses of the GCs computed allowing for the metallicity and density dependent IMF are larger than

the ones calculated using the canonical IMF (Paper I) by a factor of up to $\approx 10^2$. This also increases the number of CCSNe required to explain the observed iron abundance spreads, as more iron needs to be produced to pollute the more massive gas cloud.

(2) The computed mass function power-law index α_3 for high-mass stars ($m > 1M_{\odot}$) is smaller than 2.3 for all GCs, which means that all GCs had IMFs that were more top-heavy than the canonical one. This decreases the time until SF ends since the fraction of massive stars is larger and therefore a larger portion of the CCSNe are from massive, short-lived stars (Dabringhausen et al. 2012). According to our model, for the majority of Galactic GCs within the studied sample, the SF ended after 3.5 to 4.0 Myr after their birth. A larger portion of massive stars would also mean that the number of neutron stars and black holes created from the cluster stars is increased. In the present study we find on average 36 times as many neutron stars (NSs) and black holes (BHs) being formed compared to the results assuming a canonical IMF for all GCs. The most extreme case in this study, Terzan 8, produces 403 times as many neutron stars and black holes than it would with a canonical IMF.

(3) Both the lower and the upper limit for the initial GC mass is largest close to the Galactic centre and declines with the Galactocentric radius. The first finding is easily explained as GCs near the Galactic centre dissolve quicker due to the stronger gravitational field. The second finding points towards more massive GCs having formed closer to the Galactic centre than further away (see also Pflamm-Altenburg et al. 2013). To determine if this is a general trend for GC masses within galaxies, more GC systems need to be analysed. This would give us valuable information to determine whether or not GCs were formed in-situ and thus during the earliest assembly phase of the Galaxy with implications for the formation of super-massive black holes (Kroupa et al. 2020). The monolithic-collapse-model for the formation of galaxy spheroids, bulges and elliptical galaxies implies that the most massive clusters form in the innermost regions of the later galaxy. These can appear as quasars (Jeřábková et al. 2017). In this model, the mass of the most-massive central star cluster correlates with the mass of the final galaxy. While the formation of the galaxy occurs on the down-sizing time, the central star cluster’s stellar black holes are compressed into a relativistic state by the in-falling gas. They form, within a few hundred Myr, a super-massive black hole through gravitational-wave-emission-driven collapse of the central stellar-black-hole system (Kroupa et al. 2020).

ACKNOWLEDGEMENTS

We want to thank an anonymous referee for their useful comments. The authors acknowledge support from the Grant Agency of the Czech Republic under grant number 20-21855S and through the DAAD-Eastern-Europe Exchange grant at Bonn University. Z.Y. acknowledges support from the Fundamental Research Funds for the Central Universities under grant number 0201/14380049. Z.Y. acknowledges support through the Jiangsu Funding Program for Excellent Postdoctoral Talent under grant number 20220ZB54. Z.Y. acknowledges the support of the National Natural Science Foundation of China (NSFC) under grants No. 12041305 and

12173016. Z.Y. acknowledges the science research grants from the China Manned Space Project with NO.CMS-CSST-2021-A08 (IMF).

DATA AVAILABILITY

The data used here has been cited and is available in published form.

REFERENCES

- Aarseth S. J., Tout C. A., Mardling R. A., 2008, *The Cambridge N-Body Lectures*. Vol. 760, doi:10.1007/978-1-4020-8431-7,
- André P., Di Francesco J., Ward-Thompson D., Inutsuka S. I., Pudritz R. E., Pineda J. E., 2014, in Beuther H., Klessen R. S., Dullemond C. P., Henning T., eds, *Protostars and Planets VI*. p. 27 (arXiv:1312.6232), doi:10.2458/azu_uapress_9780816531240-ch002
- Ashman K. M., Zepf S. E., 2001, *AJ*, 122, 1888
- Asplund M., Grevesse N., Sauval A. J., Scott P., 2009, *ARA&A*, 47, 481
- Bailin J., 2019, *ApJS*, 245, 5
- Bailin J., von Klar R., 2022, *ApJ*, 925, 36
- Banerjee S., Kroupa P., 2011, *ApJ*, 741, L12
- Banerjee S., Kroupa P., 2018, *Formation of Very Young Massive Clusters and Implications for Globular Clusters*. p. 143, doi:10.1007/978-3-319-22801-3_6
- Basinger C. M., Kochanek C. S., Adams S. M., Dai X., Stanek K. Z., 2020, arXiv e-prints, p. arXiv:2007.15658
- Bastian N., Lardo C., 2015, *MNRAS*, 453, 357
- Bastian N., Strader J., 2014, *MNRAS*, 443, 3594
- Baumgardt H., 2001, *MNRAS*, 325, 1323
- Baumgardt H., Makino J., 2003, *MNRAS*, 340, 227
- Baumgardt H., Kroupa P., Parmentier G., 2008, *MNRAS*, 384, 1231
- Baumgardt H., Hilker M., Sollima A., Bellini A., 2019, *MNRAS*, 482, 5138
- Bekki K., Freeman K. C., 2003, *MNRAS*, 346, L11
- Bekki K., Jeřábková T., Kroupa P., 2017, *MNRAS*, 471, 2242
- Brinkmann N., Banerjee S., Motwani B., Kroupa P., 2017, *A&A*, 600, A49
- Calura F., Few C. G., Romano D., D’Ercole A., 2015, *ApJ*, 814, L14
- Carney B. W., 1996, *PASP*, 108, 900
- Carretta E., et al., 2009a, *A&A*, 505, 117
- Carretta E., Bragaglia A., Gratton R., D’Orazi V., Lucatello S., 2009b, *A&A*, 508, 695
- Carretta E., Lucatello S., Gratton R. G., Bragaglia A., D’Orazi V., 2011, *A&A*, 533, A69
- Carretta E., Bragaglia A., Gratton R. G., Lucatello S., D’Orazi V., 2012, *ApJ*, 750, L14
- Carretta E., et al., 2013, *A&A*, 557, A138
- Carretta E., et al., 2014, *A&A*, 564, A60
- Carretta E., et al., 2015, *A&A*, 578, A116
- Chon S., Omukai K., Schneider R., 2021, arXiv e-prints, p. arXiv:2103.04997
- Cohen R. E., Bellini A., Casagrande L., Brown T. M., Correnti M., Kalirai J. S., 2021, arXiv e-prints, p. arXiv:2109.08708
- Corbelli E., 2003, *MNRAS*, 342, 199
- D’Antona F., Vesperini E., D’Ercole A., Ventura P., Milone A. P., Marino A. F., Tailo M., 2016, *MNRAS*, 458, 2122
- Dabringhausen J., Kroupa P., Baumgardt H., 2009, *MNRAS*, 394, 1529
- Dabringhausen J., Kroupa P., Pflamm-Altenburg J., Mieske S., 2012, *ApJ*, 747, 72
- Dale J. E., Ercolano B., Bonnell I. A., 2012, *MNRAS*, 424, 377
- Deason A. J., Belokurov V., Sanders J. L., 2019, *MNRAS*, 490, 3426
- Dotter A., et al., 2010, *ApJ*, 708, 698
- Fall S. M., Zhang Q., 2001, *ApJ*, 561, 751
- Farrell E., Groh J. H., Meynet G., Eldridge J. J., 2022, *MNRAS*,
- Ferraro F. R., et al., 2009, *Nature*, 462, 483
- Forbes D. A., Spitler L. R., Strader J., Romanowsky A. J., Brodie J. P., Foster C., 2011, *MNRAS*, 413, 2943
- Gilmore G., Wyse R. F. G., 1998, *AJ*, 116, 748
- Gürkan M. A., Freitag M., Rasio F. A., 2004, *ApJ*, 604, 632
- Haghi H., Safaei G., Zonoozi A. H., Kroupa P., 2020, *ApJ*, 904, 43
- Han D., Kimm T., Katz H., Devriendt J., Slyz A., 2022, arXiv e-prints, p. arXiv:2207.05745
- Harris W. E., Harris G. L. H., Alessi M., 2013, *ApJ*, 772, 82
- Heger A., Woosley S. E., Fryer C. L., Langer N., 2003a, in Hillebrandt W., Leibundgut B., eds, *From Twilight to Highlight: The Physics of Supernovae*. p. 3 (arXiv:astro-ph/0211062), doi:10.1007/10828549_1
- Heger A., Fryer C. L., Woosley S. E., Langer N., Hartmann D. H., 2003b, *ApJ*, 591, 288
- Heggie D., Hut P., 2003, *The Gravitational Million-Body Problem: A Multidisciplinary Approach to Star Cluster Dynamics*
- Hilker M., Baumgardt H., Sollima A., Bellini A., 2019, *Proceedings of the International Astronomical Union*, 14, 451–454
- Jerabkova T., Boffin H. M. J., Beccari G., de Marchi G., de Bruijne J. H. J., Prusti T., 2021, *A&A*, 647, A137
- Jeřábková T., Kroupa P., Dabringhausen J., Hilker M., Bekki K., 2017, *A&A*, 608, A53
- Jeřábková T., Hasani Zonoozi A., Kroupa P., Beccari G., Yan Z., Vazdekis A., Zhang Z. Y., 2018, *A&A*, 620, A39
- Joshi K. J., Nave C. P., Rasio F. A., 2001, *ApJ*, 550, 691
- Kacharov N., Koch A., McWilliam A., 2013, *A&A*, 554, A81
- Kafle P. R., Sharma S., Lewis G. F., Bland-Hawthorn J., 2012, *ApJ*, 761, 98
- Kalari V. M., Carraro G., Evans C. J., Rubio M., 2018, *ApJ*, 857, 132
- Krause M. G. H., Charbonnel C., Bastian N., Diehl R., 2016, *A&A*, 587, A53
- Kravtsov V., Dib S., Calderón F. A., Belinchón J. A., 2022, *MNRAS*, 512, 2936
- Kroupa P., 2001, *MNRAS*, 322, 231
- Kroupa P., 2002, *Science*, 295, 82
- Kroupa P., Tout C. A., Gilmore G., 1993, *MNRAS*, 262, 545
- Kroupa P., Weidner C., Pflamm-Altenburg J., Thies I., Dabringhausen J., Marks M., Maschberger T., 2013, *The Stellar and Sub-Stellar Initial Mass Function of Simple and Composite Populations*. Springer Netherlands, p. 115, doi:10.1007/978-94-007-5612-0_4
- Kroupa P., Subr L., Jerabkova T., Wang L., 2020, *MNRAS*, 498, 5652
- Lacchin E., Calura F., Vesperini E., 2021, *MNRAS*, 506, 5951
- Lada C. J., Lada E. A., 2003, *ARA&A*, 41, 57
- Lamers H. J. G. L. M., Baumgardt H., Gieles M., 2010, *MNRAS*, 409, 305
- Lardo C., Mucciarelli A., Bastian N., 2016, *MNRAS*, 457, 51
- Lardo C., Salaris M., Cassisi S., Bastian N., 2022, arXiv e-prints, p. arXiv:2205.03323
- Mahani H., Zonoozi A. H., Haghi H., Jeřábková T., Kroupa P., Mieske S., 2021, *MNRAS*, 502, 5185
- Maoz D., Graur O., 2017, *ApJ*, 848, 25
- Marigo P., 2001, *A&A*, 370, 194
- Marino A. F., et al., 2015, *MNRAS*, 450, 815
- Marino A. F., et al., 2018, *ApJ*, 859, 81
- Marino A. F., et al., 2019, *MNRAS*, 487, 3815
- Marks M., Kroupa P., 2012, *A&A*, 543, A8
- Marks M., Kroupa P., Dabringhausen J., Pawlowski M. S., 2012, *MNRAS*, 422, 2246

Marks M., Kroupa P., Dabringhausen J., 2022, *A&A*, 659, A96

Marquardt D. W., 1963, *Journal of the Society for Industrial and Applied Mathematics*, 11, 431

Massari D., et al., 2014, *ApJ*, 795, 22

McMillan P. J., 2011, *MNRAS*, 414, 2446

McMillan P. J., 2017, *MNRAS*, 465, 76

Megeath S. T., et al., 2016, *AJ*, 151, 5

Montecinos C., Villanova S., Muñoz C., Cortés C. C., 2021, arXiv e-prints, p. arXiv:2103.07014

Mucciarelli A., Lapenna E., Massari D., Pancino E., Stetson P. B., Ferraro F. R., Lanzoni B., Lardo C., 2015, *ApJ*, 809, 128

Neustadt J. M. M., Kochanek C. S., Stanek K. Z., Basinger C. M., Jayasinghe T., Garling C. T., Adams S. M., Gerke J., 2021, arXiv e-prints, p. arXiv:2104.03318

Nomoto K., Kobayashi C., Tominaga N., 2013, *ARA&A*, 51, 457

Pancino E., Ferraro F. R., Bellazzini M., Piotto G., Zoccali M., 2000, *ApJ*, 534, L83

Parmentier G., Jehin E., Magain P., Neuforge C., Noels A., Thoul A. A., 1999, *A&A*, 352, 138

Pejcha O., Thompson T. A., 2015, *ApJ*, 801, 90

Pflamm-Altenburg J., González-Lópezlira R. A., Kroupa P., 2013, *MNRAS*, 435, 2604

Portegies Zwart S. F., Boekholt T. C. N., 2018, *Communications in Nonlinear Science and Numerical Simulations*, 61, 160

Portinari L., Chiosi C., Bressan A., 1998, *A&A*, 334, 505

Pouteau Y., et al., 2022, arXiv e-prints, p. arXiv:2203.03276

Prantzos N., Charbonnel C., 2006, *A&A*, 458, 135

Regős E., Tout C. A., Wickramasinghe D., Hurley J. R., Pols O. R., 2003, *New A*, 8, 283

Renzini A., Marino A. F., Milone A. P., 2022, arXiv e-prints, p. arXiv:2203.03002

Schneider F. R. N., et al., 2018, *Science*, 359, 69

Sharda P., Krumholz M. R., 2022, *MNRAS*, 509, 1959

Sharma S., Corbelli E., Giovanardi C., Hunt L. K., Palla F., 2011, *A&A*, 534, A96

Stein S. K., 1977, *Mathematics Magazine*, 50, 160

Sukhbold T., Ertl T., Woosley S. E., Brown J. M., Janka H. T., 2016, *ApJ*, 821, 38

Usher C., Brodie J. P., Forbes D. A., Romanowsky A. J., Strader J., Pfeffer J., Bastian N., 2019, *MNRAS*, 490, 491

Verliat A., Hennebelle P., González M., Lee Y.-N., Geen S., 2022, arXiv e-prints, p. arXiv:2202.02237

Wang L., Jerabkova T., 2021, *A&A*, 655, A71

Webb J. J., Bovy J., 2021, arXiv e-prints, p. arXiv:2108.02217

Webb J. J., Leigh N. W. C., 2015, *MNRAS*, 453, 3278

Willson L. A., 2000, *ARA&A*, 38, 573

Wirth H., Jerabkova T., Yan Z., Kroupa P., Haas J., Šubr L., 2021, *MNRAS*, 506, 4131

Yan Z., Jerabkova T., Kroupa P., 2017, *A&A*, 607, A126

Yan Z., Jerabkova T., Kroupa P., Vazdekis A., 2019, *A&A*, 629, A93

Yan Z., Jerabkova T., Kroupa P., 2020, *A&A*, 637, A68

Yan Z., Jeřábková T., Kroupa P., 2021, *A&A*, 655, A19

Zhang Z.-Y., Romano D., Ivison R. J., Papadopoulos P. P., Matteucci F., 2018, *Nature*, 558, 260

APPENDIX A: COMPUTING THE LIMITING FUNCTIONS FROM POINT CLOUDS

In this work the limiting functions to a number of point clouds has been computed (see Figs. 4 to 8). All of these limiting functions are computed in log-log-space ($x' = \log(x)$ and $y' = \log(y)$) and under the assumption that the function takes the form $y' = a + bx'$ in this space. The method will be demonstrated for the case of finding a maximum function with a positive slope to a point cloud as visible in Fig. A1

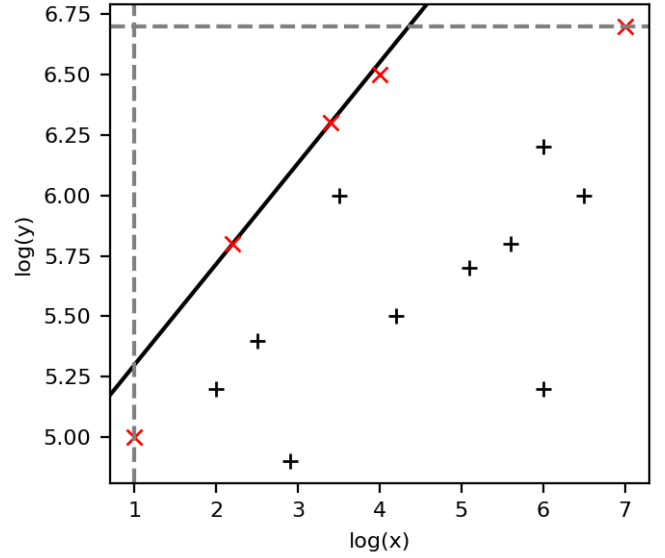


Figure A1. An example of a limiting function for the maximal values of a pointcloud given by the red and black crosses.

and then discuss how this algorithm can be generalized. The algorithm attempts to find a line that satisfies two conditions:

- (1) no point is allowed left of the line,
- (2) the area enclosed between the found line and the line marking the minimum x-value, x'_{\min} , and maximum y-value, y'_{\max} , (shown as dashed lines in Fig. A1) shall be maximised. Henceforth, we will call this area the ‘empty triangle’.

From the second condition we can conclude, that the line must go through at least one point of the point cloud. Otherwise we can always find a line parallel to the chosen one, that has all points to its right and produces a larger empty triangle. Therefore, we start by determining which points out of our point cloud are relevant for our calculations. These are all the points, through which we can put a line such that condition (1) is fulfilled. They are marked with red ‘x’s in Fig. A1.

A linear function through a Point $P = (x'_P, y'_P)$ can be written as:

$$y'_P = a + bx'_P. \quad (\text{A1})$$

Solving this equation for a we can now express the area, A , of the empty triangle depending on the slope b :

$$A = \frac{1}{2} (y'_{\max} - y'_P - b(x'_{\min} - x'_P)) \left(\frac{y'_{\max} - y'_P}{b} + x'_P - x'_{\min} \right). \quad (\text{A2})$$

It is easy to compute that for $A > 0$ this function has one global minimum at $b_{\min} = \frac{y'_{\max} - y'_P}{x'_P - x'_{\min}}$. It is monotonic decreasing for $0 < b < b_{\min}$ and monotonic increasing for $b_{\min} < b$.

Due to condition (1) the minimum possible b for a line through one of the relevant points is the one for which the line goes through its right neighbour and the maximum possible b is the one for which its line goes through its left neighbour. For the relevant points with the lowest and highest x' only the line to one neighbour (the only one they have) has to be taken into account since all other possible lines with positive

b that fulfil (1) lead to a smaller empty triangle. Therefore, by comparing the areas of the empty triangles created by the connections between all the neighbouring relevant points the function fulfilling both (1) and (2) can be found. The connection producing the largest area is the solution.

Analogously a minimum function can be found by maximizing the triangle between $y' = y'_{\min}$ and $x' = x'_{\max}$ and the target function. For a negative slope, b , $x' = x'_{\max}$ and $y' = y'_{\max}$ can be used to find the maximum function and $x' = x'_{\min}$ and $y' = y'_{\min}$ can be used to find the minimum function.

This paper has been typeset from a $\text{\TeX}/\text{\LaTeX}$ file prepared by the author.